Higgs self-coupling determination in the bb$\gamma\gamma$ final state at the FCC-hh

Paola Mastrapasqua[1*], Angela Taliercio[2*], Birgit Stapf[3*] and Michele Selvaggi[1*]

[1]Centre for Cosmology, Particle Physics and Phenomenology (CP3), Université catholique de Louvain, Louvain-la-Neuve, Belgium.
[2]Northwestern University, Evanston, Illinois, USA.
[3,4]CERN, Geneva, Switzerland.

*Corresponding author(s). E-mail(s): paola.mastrapasqua@cern.ch; angela.taliercio@cern.ch; birgit.stapf@cern.ch; michele.selvaggi@cern.ch;

1 Introduction

The study of Higgs boson pair production is one of the key benchmarks of the scientific program at future colliders. It offers direct experimental access to the Higgs boson trilinear self-coupling and hence to the structure of the scalar potential itself, allowing unprecedented insight into the electroweak symmetry breaking mechanism. The self-coupling modifier κ_λ, defined as the ratio of the measured value of the self-coupling over its Standard Model (SM) predicted value - λ/λ_{SM} - is used to parameterize any deviation from the SM expectations. A precision measurement of κ_λ down to the percent level is a clear goal for future experiments, as at the end of the HL-LHC era the κ_λ precision is expected to reach only around 30%. In the SM, Higgs pair production events in hadron collisions are a rare occurrence - with the production cross-section for a Higgs pair in the dominant gluon-gluon fusion mode being three orders of magnitude smaller than that to produce a single Higgs boson [1].

The hadron collider phase of the Future Circular Collider (FCC-hh) would be a proton-proton collider operating at a center-of-mass energy of 80-100 TeV. It is one of the most ambitious projects planned for the rest of this century and offers ample opportunities in the hunt for new physics, both through its direct detection reach as well as through precision measurements. With the large data set of 30 ab^{-1}, which is envisioned to be collected during the FCC-hh runtime, the Higgs self-coupling could potentially be determined down to the percent level.

Previous projections on κ_λ were obtained in Ref. [2] at 100 TeV, where three final states were considered, $b\bar{b}\gamma\gamma$, $b\bar{b}\tau\tau$ and $b\bar{b}b\bar{b}$, achieving a projected sensitivity of 3.4%–7.8% on κ_λ, depending on the assumed detector performance and systematic uncertainties, and driven mainly by the $b\bar{b}\gamma\gamma$ final state.

In the present study, we investigate the expected precision measurement on κ_λ and on the signal strength $\mu = \sigma/\sigma_{SM}$, exploiting the most sensitive final state, $b\bar{b}\gamma\gamma$, using a more sophisticated analysis strategy. The explored center-of-mass energy hypotheses are 84, 100 and 120 TeV [3], while the detector is the nominal one for FCC-hh, as described in the conceptual design report [4, 5]. The expected integrated luminosity corresponds to 30 ab^{-1} for 84 and 100 TeV, and to 12 ab^{-1} for 120 TeV. The results are also presented for different di-jet invariant mass resolution assumptions and different systematic uncertainty scenarios.

2 Event Generation

The studies reported here rely on simulated event samples generated by the MadGraph_aMCatNLO [6], Powheg and Pythia8 [7] Monte Carlo (MC) programs, and processed through the fast detector simulation package Delphes [8]. The baseline detector concept used for the FCC-hh physics studies is described in Ref. [5, 9] and its parameterisation Delphes in Ref. [10]. The event samples have been produced with the Key4Hep framework [11, 12]. The complete list of generated samples can be found in Ref. [13].

Di-Higgs production signal samples for the SM and Beyond SM (BSM) hypotheses with different values (1, 2.45, and 3) of κ_λ are simulated to study the expected precision. The corresponding Feynman diagrams are shown in Figure 1. Only gluon-fusion HH production is considered here. Including the ttHH, VHH and VBF-HH production has the potential to further improve the expected precision estimated with this study. The backgrounds considered for the study can be divided into two groups: resonant processes, where a single Higgs boson decays to photons, and non-resonant processes, where no physical Higgs bosons are produced. The main resonant background sources are the single-Higgs processes produced via gluon-gluon fusion and in associated production with top pairs. The non-resonant background consists of QCD events containing two isolated, energetic photons. The Table 1 reports the simulated processes with related cross-section and k-factor values.

3 Analysis Strategy

The analysis strategy consists of kinematic selections to identify the Higgs boson candidates, implementation of multivariate classifiers to improve the signal-to-background ratio, event categorization, and extraction of results from the di-photon invariant mass fit in bins of the di-jet mass.

Jets are reconstructed using the anti-kT algorithm with a size radius of 0.4 [14]. Jets are selected to have a minimum p_T of 30 GeV, a maximum $|\eta|$ of 4 and to pass the medium b-tagging working point. The two highest-p_T jets are chosen to build the $H \to bb$ candidate. Photons are required to have, as well, $p_\mathrm{T} > 30$ GeV and $|\eta| <4$. The two highest-p_T photons are chosen to build the $H \to \gamma\gamma$ candidate. The invariant

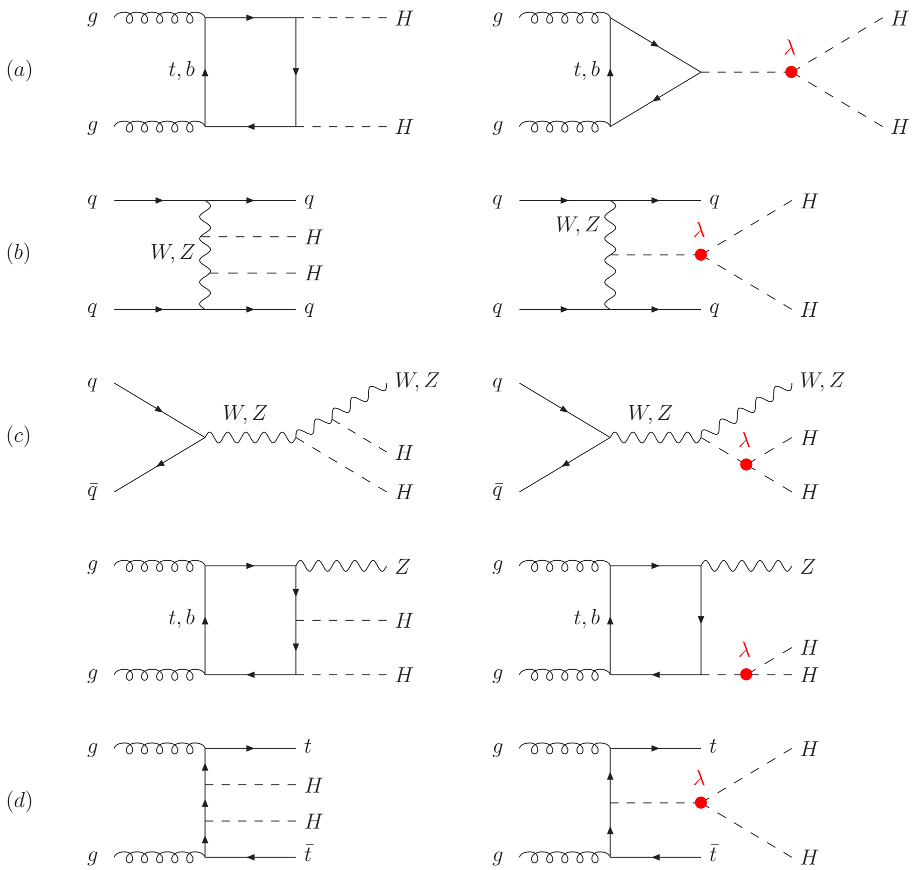

Fig. 1: Diagrams contributing to Higgs pair production: (a) gluon fusion, (b) vector-boson fusion, (c) double Higgs-strahlung and (d) double Higgs bremsstrahlung off top quarks. The trilinear Higgs self-coupling is marked in red.

mass of the jet pair is required to be in the range [80,150] GeV, while the di-photon invariant mass in the [115,135] GeV one.

Figure 2 shows the di-photon and di-jet mass distributions after the baseline selection for the di-Higgs production process (both SM and BSM) and the backgrounds, at 84 TeV. The di-jet mass distribution corresponds to the nominal Delphes one, without any mass regression. In the improved scenarios, we hypothesize a gaussian-like shape for the di-jet mass with 125 GeV mean and resolution of 10 GeV, 5 GeV and, in the most ambitious case, of 3 GeV. In these scenarios, a cut [100,150] GeV is applied on the di-jet mass.

After the baseline selection, a Deep Neural Network (DNN) is trained to discriminate the signal (both SM and BSM) against the backgrounds. Several kinematic and angular variables are used in the training, exploiting the peculiar topology of

Process	Cross-section × BR [fb]			k-factor
	84 TeV	100 TeV	120 TeV	
Signals				
$ggHH$, $\kappa_\lambda = 1$	2.33	2.98	3.91	1.08
$ggHH$, $\kappa_\lambda = 2.4$	1.03	1.29	1.75	1.08
$ggHH$, $\kappa_\lambda = 3$	1.22	1.55	2.04	1.08
Backgrounds				
Single-Higgs				
ggH	1057	1334	1699	3.76
VBF H	153	191	239	4.3
$t\bar{t}H$	74	102	140	1.22
VH	69	85	105	1.32
Non-resonant di-photon				
$\gamma\gamma jj$	14340	17970	22440	1.2

Table 1: Overview of signal and background samples with their cross sections at 84, 100 and 120 TeV.

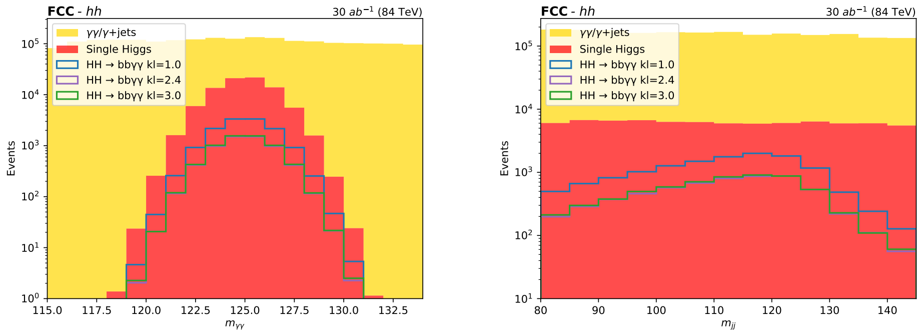

Fig. 2: Di-photon (left) and di-jet (right) invariant mass after the baseline selection.

the di-Higgs production with respect to the single-Higgs events and the non-resonant background. The input features are described in Appendix A.

The DNN score is used to define three purity regions. The low-purity region is simply discarded, whereas the medium- and high-purity regions become two separate categories. The exact values of the cuts are chosen through an optimization procedure aiming to maximize the significance $S/\sqrt{(B)}$.

Tables 2, 3 and 4 report the yields after the baseline selection and the DNN cut (low-purity region removal) with relative efficiencies, for the investigated center-of-mass energies. For this study we assumed, very conservatively, a total non-resonant background which is twice the simulated $\gamma\gamma jj$ process, to account for QCD events where only one photon is produced ($\gamma+$ jets). The background with highest pre-selection efficiency is the ttH process, which contains two real b-jets. Nonetheless, the DNN efficiently separates the ttH process from the di-Higgs production; as a result, the selected DNN cut reduces this background by $\simeq$50%, while having minimal impact on the signal.

Process (84 TeV, 30 ab^{-1})	No Sel.	Pre-Sel.	Eff.	After DNN	Rel.Eff.	Tot. Eff.
$ggHH$, $\kappa_\lambda = 1$	75289	13469	17.89%	11695	86.83%	15.53%
$ggHH$, $\kappa_\lambda = 2.4$	33142	6068	18.31%	54276	89.44%	16.37%
$ggHH$, $\kappa_\lambda = 3$	39488	6288	15.92%	5735	91.21%	14.52%
single-Higgs, ggH	44725622	19986	0.04%	12782	63.95%	0.03%
single-Higgs, VBF H	3707204	4199	0.11%	2558	60.92%	0.07%
single-Higgs, $t\bar{t}H$	1684404	58070	3.45%	29441	50.70%	1.75%
single-Higgs, VH	1517891	3594	0.24%	3221	89.62%	0.21%
Non-res ($\gamma\gamma jj\times$ 2)	1032480000	2130008	0.21%	415448	66.45%	0.14%

Table 2: Yields table with selection efficiencies at 84 TeV, considering 30 ab^{-1} of integrated luminosity.

Process (100 TeV, 30 ab^{-1})	No Sel.	Pre-Sel.	Eff.	After DNN	Rel.Eff.	Tot. Eff.
$ggHH$, $\kappa_\lambda = 1$	96280	16928	17.58%	14163	83.67%	14.71%
$ggHH$, $\kappa_\lambda = 2.4$	41517	7473	18.00%	6574	87.98%	15.84%
$ggHH$, $\kappa_\lambda = 3$	49905	7777	15.58%	6968	89.60%	13.96%
single-Higgs, ggH	54757576	23253	0.04%	11732	50.45%	0.02%
single-Higgs, VBF H	4633730	5396	0.12%	2266	42.00%	0.05%
single-Higgs, $t\bar{t}H$	2283668	76460	3.35%	38000	49.70%	1.66%
single-Higgs, VH	1833738	4361	0.24%	3748	85.94%	0.20%
Non-res ($\gamma\gamma jj\times$ 2)	1293840000	2703137	0.21%	1356627	50.19%	0.10%

Table 3: Yields table with selection efficiencies at 100 TeV, considering 30 ab^{-1} of integrated luminosity.

Process (120 TeV, 12 ab^{-1})	No Sel.	Pre-Sel.	Eff.	After DNN	Rel.Eff.	Tot. Eff.
$ggHH$, $\kappa_\lambda = 1$	50493	8679	17.19%	7064	81.39%	13.99%
$ggHH$, $\kappa_\lambda = 2.4$	22582	4055	17.96%	3467	85.49%	15.35%
$ggHH$, $\kappa_\lambda = 3$	26332	4075	15.47%	3547	87.06%	13.47%
single-Higgs, ggH	27206334	13385	0.05%	8010	59.84%	0.03%
single-Higgs, VBF H	2334447	2896	0.12%	1582	54.64%	0.07%
single-Higgs, $t\bar{t}H$	1238352	40634	3.28%	17589	43.29%	1.42%
single-Higgs, VH	884717	2145	0.24%	1846	86.06%	0.21%
Non-res ($\gamma\gamma jj\times$ 2)	646272000	1390237	0.22%	834314	60.01%	0.13%

Table 4: Yields table with selection efficiencies at 120 TeV, considering 12 ab^{-1} of integrated luminosity.

Another categorization is based on the corrected di-Higgs invariant mass (visible in left Figure 3), $M_x = m_{\gamma\gamma jj} - m_{\gamma\gamma} - m_{jj} + 250\text{GeV}$, and separates the region where the SM dominates ($M_x > 350$ GeV) from the one where BSM signals have higher contribution ($M_x < 350\text{GeV}$).

The high-M_x category is the one driving the sensitivity for the SM assumption. Right Figure 3 shows the DNN score with the cut chosen to define the medium- and high-purity regions in this high-M_x category, while Figure 4 presents the di-photon distributions in the two purity regions for this category. The yields per category are reported in Appendix B.

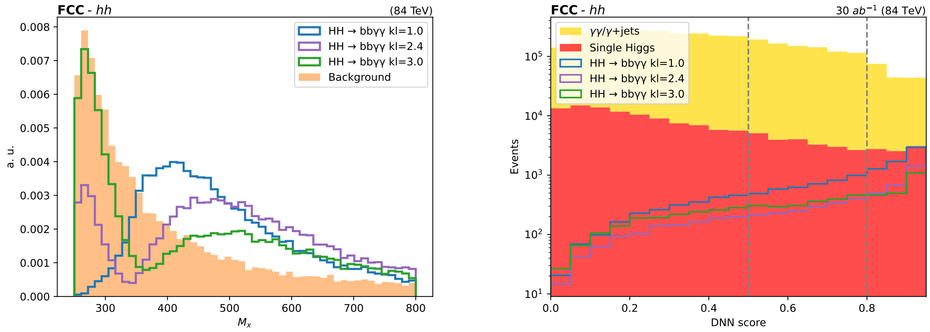

Fig. 3: M_x distribution (left) and DNN score (right) with chosen cuts for the high-M_x category.

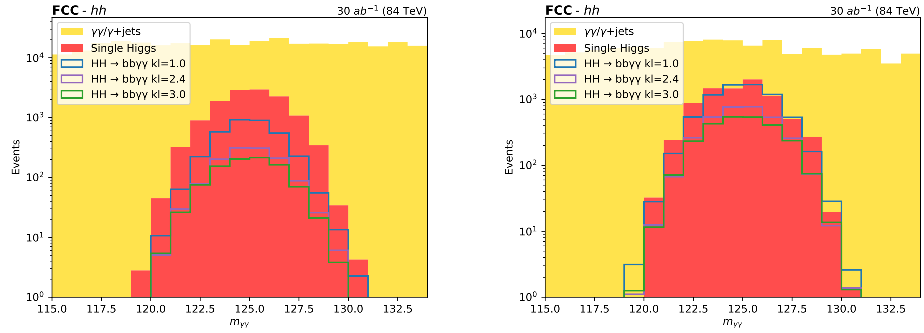

Fig. 4: Di-photon invariant mass in the medium (left) and high (right) purity regions, in the high-M_x category.

To extract the final results, a maximum likelihood fit is performed on the di-photon invariant mass distribution in few bins of the di-jet mass. The binning in di-jet mass changes with the di-jet mass resolution assumption and is chosen as a tradeoff between high sensitivity and reasonable number of simulated events in each bin. It is important to highlight that the sensitivity to different di-jet mass resolution hypotheses is highly dependent on this binning choice. In the future, a larger number of simulated events will enable finer binning and further improvements in the results.

Figure 5 shows the selected binning for the nominal Delphes scenario and the 10 GeV resolution one, in the high-purity high-M_x category. As example, Figure 6 displays the final observable in the most sensitive di-jet mass bins for the nominal scenario. In this scenario, a total of 16 regions are used to extract the final results, considering 2 M_x categories, 2 purity categories and 4 di-jet mass bins.

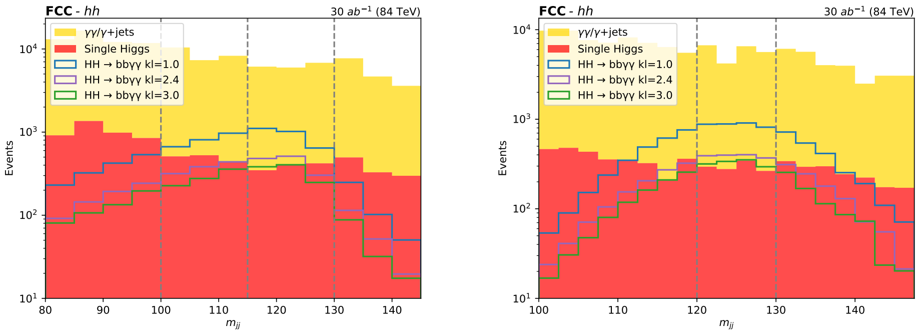

Fig. 5: Di-jet mass distribution with chosen binning in the nominal (left) and gaussian 10 GeV scenario (right), for the high-purity, high-M_x category.

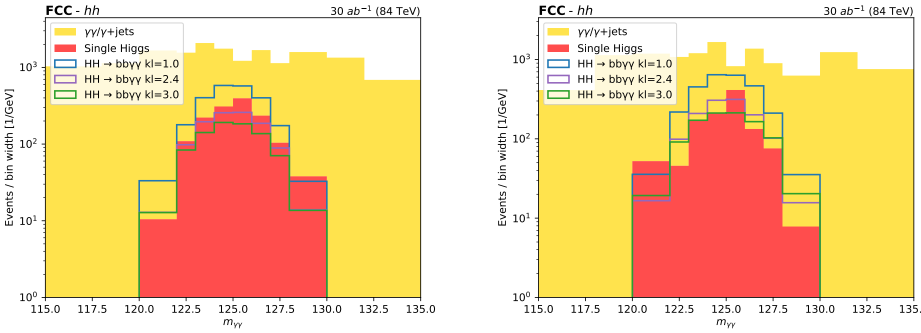

Fig. 6: Di-photon mass distribution in the most sensitive di-jet mass bins for the nominal DELPHES scenario: $[100-115]$(left) and $[115-130]$ (right). Plots refers to high-purity, high-M_x category.

4 Results

The determination of the Higgs self-coupling modifier κ_λ is performed for three different benchmarks of systematic uncertainties, as listed in Table 5. These benchmarks have different instrumental uncertainties assumptions, while sharing the same background normalization uncertainty treatment. The non-resonant background is estimated from the sidebands of the $\mathrm{m}_{\gamma\gamma}, \mathrm{m}_{\mathrm{bb}}$ spectrum, hence its normalization is left free to float within 5% and is effectively constrained in the fit to 1%. For the single-Higgs background, although possibly estimated from data in the future, no dedicated control regions are defined here, therefore it is considered as derived from simulation. A normalization uncertainty of 1% is assigned to each single-Higgs process. In this study, no hypothesis on the theoretical uncertainty of signal cross section is made, due to the difficulty of justifying a reasonable value. The systematics assumptions in scenario 3 are very conservative, and they get constrained in the fit.

Source of uncertainty	Value			Type	Applies to
	Syst. 1	Syst. 2	Syst. 3		
b-jet ID / b-jet	0.5%	1%	2%	lnN	Signal, single-Higgs bkgs
Photon ID / lepton	0.5%	1%	2%	lnN	Signal, single-Higgs bkgs
Luminosity	0.5%	1%	2%	lnN	Signal, single-Higgs bkgs
single-Higgs norm.	1%	1%	1%	lnN	single-Higgs bkgs
Non-resonant (data driven)	5%	5%	5%	lnU	Non-resonant bkg

Table 5: Overview of the systematic uncertainties scenarios.

With these systematic uncertainty benchmarks, the expected precision on κ_λ and μ is extracted from a simultaneous binned likelihood fit of the di-photon distribution in all the categories and bins described in the previous section.

A parametrization of the di-Higgs production cross-section as a function of κ_λ is estimated and exploited to extract the final results. This parametrization has the functional form of a parabola, with a minimum at κ_λ =2.45, which corresponds to maximum interference between the box and triangle diagram contributions. To accurately determine the shape of the parabola, a fit is performed using four different κ_λ values. Additionally, to account for the varying acceptance of the different κ_λ samples, the fit is conducted using the baseline selection yields.

All the produced results are summarized in Tables 6, 7 and 8 for 84, 100 and 120 TeV, respectively. The expected likelihood scans are shown in Figure 7 at 84 TeV for the nominal di-jet mass resolution.

84 TeV (30 ab^{-1}), κ_λ precision (%)	Stat. Only	Syst. 1	Syst. 2	Syst. 3
Nominal m_{jj} resolution	3.5%	4.6%	5.2%	5.4%
Gaussian m_{jj}, 10 GeV resolution	3.2%	4.3%	5.0%	5.4%
Gaussian m_{jj}, 5 GeV resolution	2.7%	3.7%	4.3%	4.6%
Gaussian m_{jj}, 3 GeV resolution	2.4%	3.2%	3.7%	3.9%

84 TeV (30 ab^{-1}), μ precision (%)	Stat. Only	Syst. 1	Syst. 2	Syst. 3
Nominal m_{jj} resolution	2.5%	3.3%	3.7%	3.9%
Gaussian m_{jj}, 10 GeV resolution	2.3%	3.1%	3.6%	3.8%
Gaussian m_{jj}, 5 GeV resolution	1.9%	2.6%	3.0%	3.2%
Gaussian m_{jj}, 3 GeV resolution	1.7%	2.3%	2.6%	2.8%

Table 6: Expected precision on κ_λ and $\mu = \sigma/\sigma_{SM}$ at 84 TeV.

At 68% confidence level, the expected precision on κ_λ ranges from 3.2% to 5.4% at 84 TeV, from 2.8% to 4.8% at 100 TeV and from 3.2% to 6.2% at 120 TeV, depending on the di-jet mass resolution and systematic assumptions. The expected precision on μ, instead, ranges from 2.3% to 3.9% at 84 TeV, from 2.0% to 3.4% at 100 TeV and from 2.3% to 4.4% at 120 TeV. The 100 TeV machine provides the highest sensitivity, while the 84 TeV and 120 TeV scenarios yield comparable results, as the sensitivity gain from increasing the energy to 120 TeV is offset by the expected reduction in integrated luminosity.

100 TeV (30 ab^{-1}), κ_λ precision (%)	Stat. Only	Syst. 1	Syst. 2	Syst. 3
Nominal m_{jj} resolution	2.8%	4.0%	4.6%	4.8%
Gaussian m_{jj}, 10 GeV resolution	2.4%	3.5%	4.1%	4.4%
Gaussian m_{jj}, 5 GeV resolution	2.2%	3.1%	3.6%	3.9%
Gaussian m_{jj}, 3 GeV resolution	1.9 %	2.8%	3.2%	3.4%

100 TeV (30 ab^{-1}), μ precision (%)	Stat. Only	Syst. 1	Syst. 2	Syst. 3
Nominal m_{jj} resolution	2.0%	2.8%	3.2%	3.4%
Gaussian m_{jj}, 10 GeV resolution	1.7%	2.5%	2.9%	3.1%
Gaussian m_{jj}, 5 GeV resolution	1.5%	2.2%	2.6%	2.8%
Gaussian m_{jj}, 3 GeV resolution	1.4%	2.0%	2.3%	2.4%

Table 7: Expected precision on κ_λ and $\mu = \sigma/\sigma_{SM}$ at 100 TeV.

120 TeV (12 ab^{-1}), κ_λ precision (%)	Stat. Only	Syst. 1	Syst. 2	Syst. 3
Nominal m_{jj} resolution	4.0%	4.6%	5.3%	6.2%
Gaussian m_{jj}, 10 GeV resolution	3.8%	4.4%	5.1%	6.0%
Gaussian m_{jj}, 5 GeV resolution	3.3%	3.8%	4.4%	5.1%
Gaussian m_{jj}, 3 GeV resolution	2.8%	3.2%	3.8%	4.4%

120 TeV (12 ab^{-1}), μ precision (%)	Stat. Only	Syst. 1	Syst. 2	Syst. 3
Nominal m_{jj} resolution	2.9%	3.3%	3.8%	4.4%
Gaussian m_{jj}, 10 GeV resolution	2.7%	3.1%	3.6%	4.3%
Gaussian m_{jj}, 5 GeV resolution	2.3%	2.7%	3.1%	3.6%
Gaussian m_{jj}, 3 GeV resolution	2.0%	2.3%	2.7%	3.1%

Table 8: Expected precision on κ_λ and $\mu = \sigma/\sigma_{SM}$ at 120 TeV.

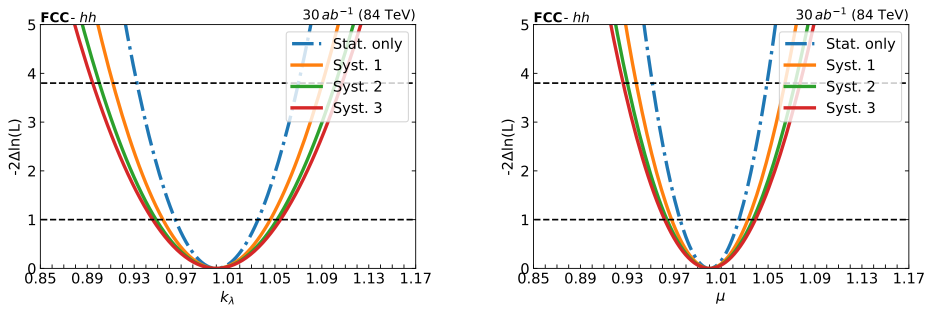

Fig. 7: Expected likelihood scans as a function of κ_λ (left) and μ (right) for different systematic uncertainty scenarios.

Figure 8 illustrates how the expected precision on κ_λ modifies as a function of center-of-mass energy and di-jet mass resolution. It can be inferred that, for instance, a 84 TeV machine with a 5 GeV resolution on di-jet mass would yield results competitive with those of a 100 TeV machine in the nominal scenario.

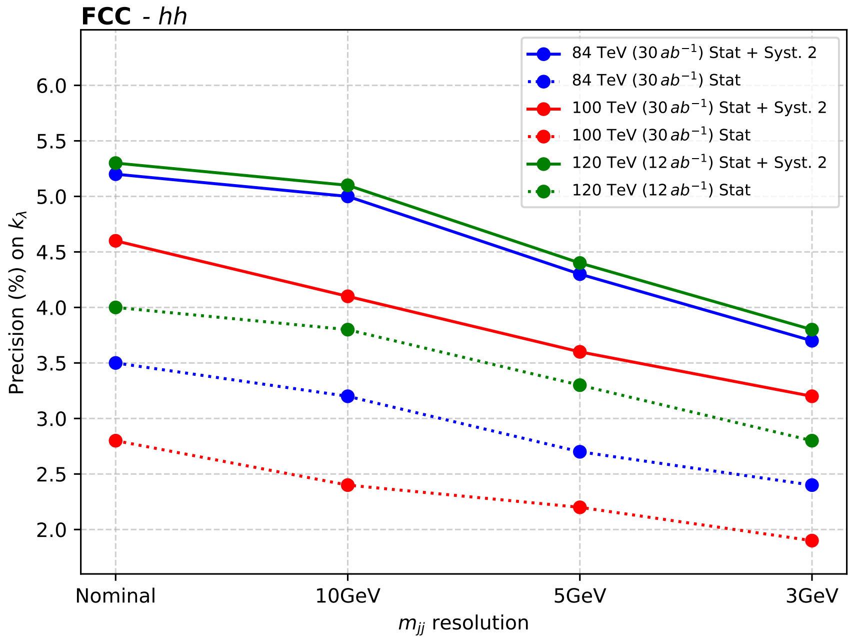

Fig. 8: Expected precision on κ_λ in the systematic scenario 2, as a function of the m_{jj} resolution and the center of mass energy.

5 Conclusion

An analysis of the prospects of the Higgs self-coupling measurement at the FCC-hh is presented, by investigating the $b\bar{b}\gamma\gamma$ final state. The $b\bar{b}\gamma\gamma$ channel represents the most sensitive di-Higgs final state, as it combines the highest Higgs branching ratio ($H \to bb$) with the high di-photon mass resolution. The expected results are shown in terms of precision on κ_λ and signal strength, for different di-jet mass resolution and systematic assumptions and different center-of-mass energies. At 84 TeV, considering an integrated luminosity of 30 ab^{-1}, the expected result lies in the range 3.2% - 5.4%. At 100 TeV, considering an integrated luminosity of 30 ab^{-1}, the range is 2.0% - 3.4%. Finally at 120 TeV, considering a lower integrated luminosity of 12 ab^{-1}, the estimated range is 3.2% - 6.2%. The study demonstrates the critical role of di-jet mass resolution in enhancing the κ_λ precision to the few-percent level, highlighting that its impact can be as significant as increasing the center-of-mass energy. Finally, it should be noted that, although $b\bar{b}\gamma\gamma$ is the leading channel, a proper combination with other di-Higgs channels, most importantly $b\bar{b}\tau\tau$ and $b\bar{b}b\bar{b}$, is essential to achieve the best possible results, with the aim of reaching the 1% precision target. Moreover, only gluon-fusion HH production was considered in this study. Including the ttHH, VHH and VBF-HH production, and designing specific event categories that enhance their contributions has the potential to further improve the expected precision presented here. Another potential improvement could possibly come from exploiting the impact of self-coupling information propagated to differential distributions, such as m_{hh} or via a dedicated MVA discriminator [15].

Acknowledgements

This work has been partly supported by the Future Circular Collider Innovation Study (FCCIS) project, that has received funding from the European Union's Horizon 2020 research and innovation programme under grant No 951754.

A DNN Input features

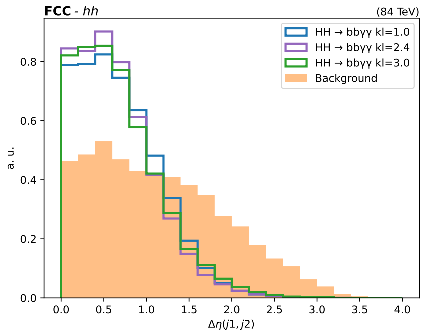

(a) $\Delta\eta$ between the jet candidates.

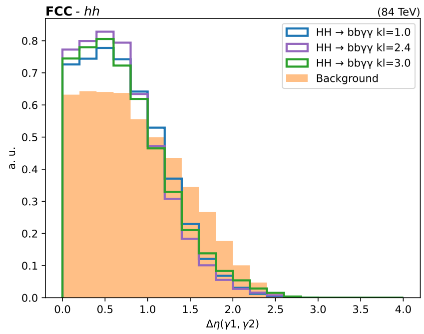

(b) $\Delta\eta$ between the photon candidates.

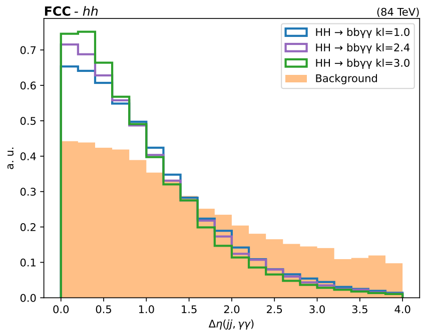

(c) $\Delta\eta$ between the Higgs candidates.

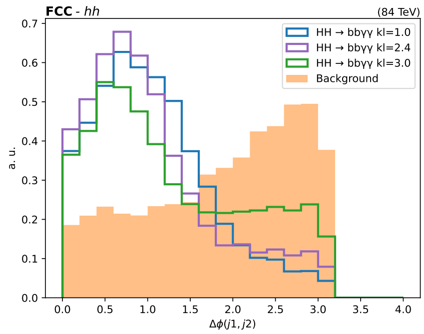

(d) $\Delta\phi$ between the jet candidates.

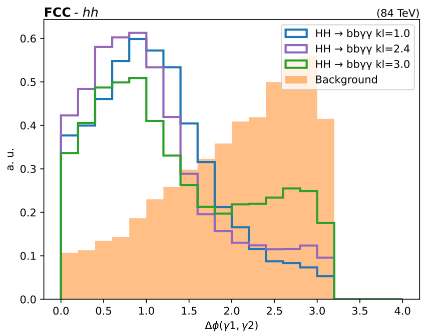

(e) $\Delta\phi$ between the photon candidates.

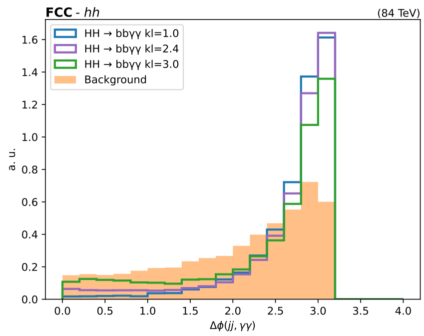

(f) $\Delta\phi$ between the Higgs candidates.

Fig. 9: DNN input features (1/3).

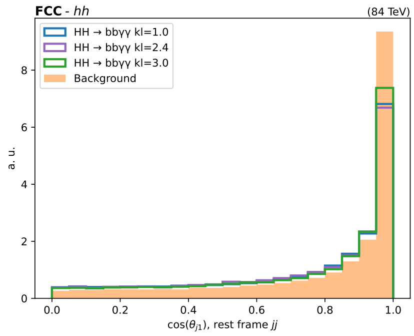

(a) Angle between the leading jet and the beam axis in the di-jet rest frame.

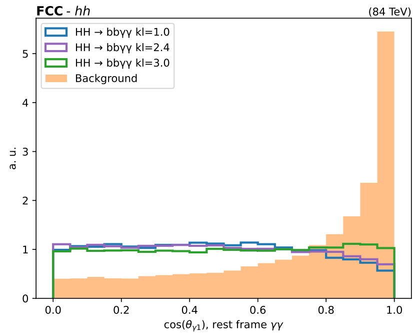

(b) Angle between the leading photon and the beam axis in the di-photon rest frame.

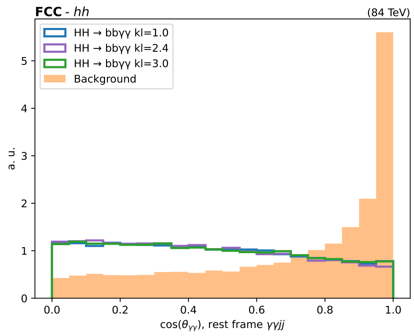

(c) Angle between the di-photon and the beam axis in the di-Higgs rest frame.

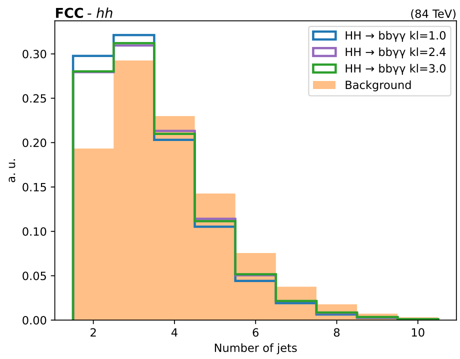

(d) Number of b-tagged jets.

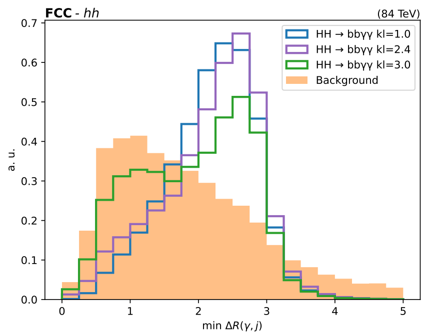

(e) ΔR between the closest photon-jet pair.

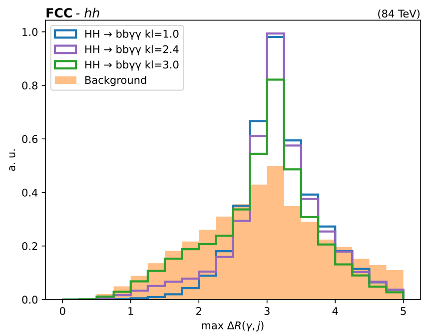

(f) ΔR between the other photon-jet pair.

Fig. 10: DNN input features (2/3).

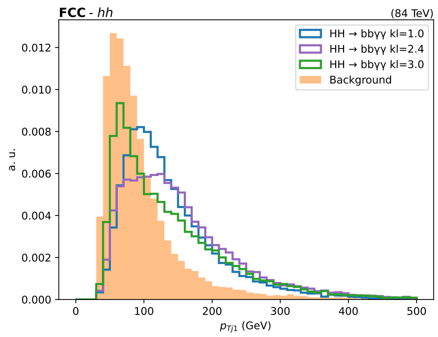

(a) p_{T} of the leading jet.

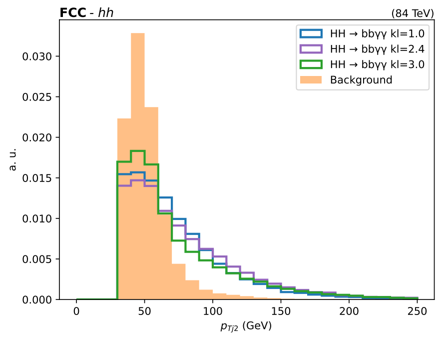

(b) p_{T} of the sub-leading jet.

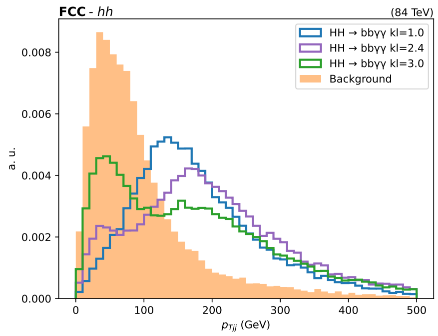

(c) p_{T} of the di-jet system.

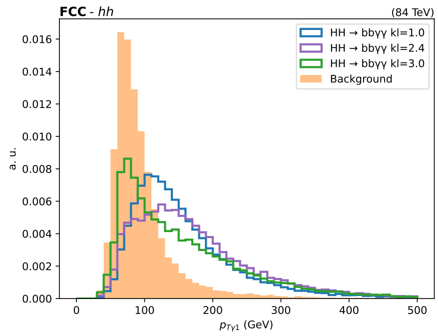

(d) p_{T} of the leading photon.

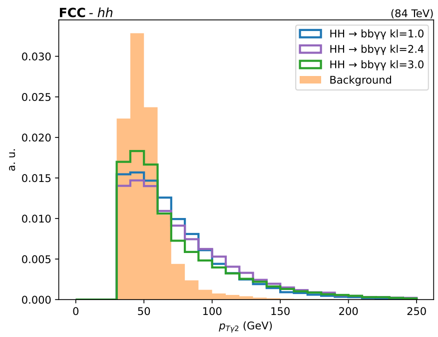

(e) p_{T} of the sub-leading photon.

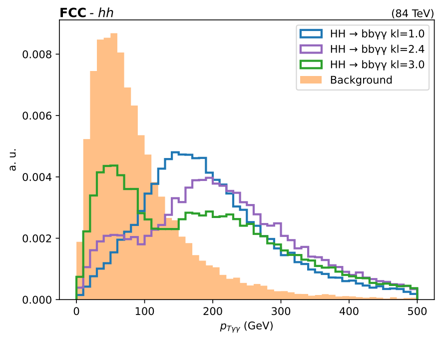

(f) p_{T} of the di-photon system.

Fig. 11: DNN input features (3/3).

B Yields divided per category

Process (84 TeV, 30 ab^{-1})	$M_x > 350$ GeV		$M_x < 350$ GeV	
	high-purity	medium-purity	high-purity	medium-purity
$ggHH$, $\kappa_\lambda = 1$	7108	3567	641	379
$ggHH$, $\kappa_\lambda = 2.4$	3287	1277	465	397
$ggHH$, $\kappa_\lambda = 3$	2512	933	1280	1009
single-Higgs, ggH	4141	4629	1700	2322
single-Higgs, VBF H	577	1249	316	415
single-Higgs, $t\bar{t}H$	1951	6060	2632	18798
single-Higgs, VH	1110	485	918	708
Non-res ($\gamma\gamma jj\times$ 2)	109840	322500	416886	566222

Table 9: Yields table divided per category at 84 TeV, considering 30 ab^{-1} of integrated luminosity.

Process (100 TeV, 30 ab^{-1})	$M_x > 350$ GeV		$M_x < 350$ GeV	
	high-purity	medium-purity	high-purity	medium-purity
$ggHH$, $\kappa_\lambda = 1$	8550	4421	847	346
$ggHH$, $\kappa_\lambda = 2.4$	3986	1560	619	410
$ggHH$, $\kappa_\lambda = 3$	3022	1151	1709	1085
single-Higgs, ggH	4211	3790	1594	2135
single-Higgs, VBF H	417	995	415	437
single-Higgs, $t\bar{t}H$	3037	9128	7264	18569
single-Higgs, VH	1221	552	1232	741
Non-res ($\gamma\gamma jj\times$ 2)	83252	210448	416404	646520

Table 10: Yields table divided per category at 100 TeV, considering 30 ab^{-1} of integrated luminosity.

Process (120 TeV, 12 ab^{-1})	$M_x > 350$ GeV		$M_x < 350$ GeV	
	high-purity	medium-purity	high-purity	medium-purity
$ggHH$, $\kappa_\lambda = 1$	10273	5933	926	525
$ggHH$, $\kappa_\lambda = 2.4$	5025	2366	748	527
$ggHH$, $\kappa_\lambda = 3$	3672	1706	2073	1414
single-Higgs, ggH	5660	8125	3004	3233
single-Higgs, VBF H	702	2002	678	572
single-Higgs, $t\bar{t}H$	2962	8975	5810	26223
single-Higgs, VH	1358	771	1708	776
Non-res ($\gamma\gamma jj\times$ 2)	133150	409336	766438	776860

Table 11: Yields table divided per category at 120 TeV, considering 30 ab^{-1} of integrated luminosity.

References

[1] B.D. Micco, M. Gouzevitch, J. Mazzitelli, C. Vernieri, Higgs boson potential at colliders: Status and perspectives. Reviews in Physics **5**, 100045 (2020). https://doi.org/https://doi.org/10.1016/j.revip.2020.100045. URL https://www.sciencedirect.com/science/article/pii/S2405428320300083

[2] M.L. Mangano, G. Ortona, M. Selvaggi, Measuring the Higgs self-coupling via Higgs-pair production at a 100 TeV p–p collider. EPJC **80**(11), 1030 (2020). https://doi.org/10.1140/epjc/s10052-020-08595-3. URL http://dx.doi.org/10.1140/epjc/s10052-020-08595-3

[3] F. Zimmermann. Scenarios for the FCC-hh (2025). https://doi.org/10.5281/zenodo.14934133

[4] A. Abada, et al., FCC-hh: The Hadron Collider: Future Circular Collider Conceptual Design Report Volume 3. EPJST **228**(4), 755–1107 (2019). https://doi.org/10.1140/epjst/e2019-900087-0

[5] M. Aleksa, et al., Conceptual design of an experiment at the FCC-hh, a future 100 TeV hadron collider **2/2022** (2022). https://doi.org/10.23731/CYRM-2022-002

[6] J. Alwall, R. Frederix, S. Frixione, V. Hirschi, F. Maltoni, O. Mattelaer, H.S. Shao, T. Stelzer, P. Torrielli, M. Zaro, The automated computation of tree-level and next-to-leading order differential cross sections, and their matching to parton shower simulations. JHEP **07**, 079 (2014). https://doi.org/10.1007/JHEP07(2014)079. arXiv:1405.0301 [hep-ph]

[7] T. Sjöstrand, S. Ask, J.R. Christiansen, R. Corke, N. Desai, P. Ilten, S. Mrenna, S. Prestel, C.O. Rasmussen, P.Z. Skands, An introduction to PYTHIA 8.2. Comput. Phys. Commun. **191**, 159 (2015). https://doi.org/10.1016/j.cpc.2015.01.024. arXiv:1410.3012 [hep-ph]

[8] de Favereau, J. and Delaere, C. and Demin, P. and Giammanco, A. and Lemaître, V. and Mertens, A. and Selvaggi, M., DELPHES 3, A modular framework for fast simulation of a generic collider experiment. JHEP **02**, 057 (2014). https://doi.org/10.1007/JHEP02(2014)057. arXiv:1307.6346 [hep-ex]

[9] A. Abada, et al., FCC-hh: The Hadron Collider: Future Circular Collider Conceptual Design Report Volume 3. Eur. Phys. J. ST **228**, 755 (2019). https://doi.org/10.1140/epjst/e2019-900087-0

[10] M. Selvaggi, B. Stapf. A Delphes parameterisation of the FCC-hh detector (2025). https://doi.org/10.17181/71pv5-tvf87

[11] B. Francois, G. Ganis, *The FCC software for PED studies* (2024). https://doi.org/10.17181/8k0c4-nkr70

[12] P. Fernandez Declara, et al., The Key4hep turnkey software stack for future colliders. PoS **EPS-HEP2021**, 844 (2022). https://doi.org/10.22323/1.398.0844

[13] B. Stapf. List of fcc_v07 official FCC-hh production samples (2025). https://doi.org/https://fcc-physics-events.web.cern.ch/fcc-hh/Delphesevents_fcc_v07/II.php

[14] M. Cacciari, G.P. Salam, G. Soyez, The anti-ktjet clustering algorithm. Journal of High Energy Physics **2008**(04), 063–063 (2008). https://doi.org/10.1088/1126-6708/2008/04/063. URL http://dx.doi.org/10.1088/1126-6708/2008/04/063

[15] B. Voirin, C. Charlot, *Extracting trilinear Higgs boson self-coupling events from HH production at the FCC-hh* (2025). https://doi.org/10.17181/6mq27-ncc26.